Journal of Sound and Vibration 329 (2010) 4980–5003

Contents lists available at ScienceDirect

Journal of Sound and Vibration

journal homepage: www.elsevier.com/locate/jsvi

Reconstruction of dynamic displacement and velocity from measured accelerations using the variational statement of an inverse problem

Yun Hwa Hong, Ho-Kyung Kim, Hae Sung Lee [*]

Department of Civil and Environmental Engineering, Seoul National University, 599 Gwanak-ro Gwanak-gu, Seoul 151-744, Republic of Korea

ARTICLE INFO

Article history:
Received 18 November 2009
Received in revised form
25 March 2010
Accepted 15 May 2010
Handling Editor: L.G. Tham
Available online 11 June 2010

ABSTRACT

This paper presents two types of finite impulse response (FIR) filters to reconstruct dynamic displacement induced by structural vibration from measured acceleration. The governing equation for the reconstruction is derived by taking the variation of a minimization problem, which defines an inverse problem on displacement. A regularization function for overcoming the ill-posedness of the inverse problem is included in the minimization problem. The governing equation of the inverse problem becomes the same type of differential equation as that of a beam on an elastic foundation. The conventional FIR (CFIR) filter directly approximates the transfer function of the governing equation, while the FEM-based FIR (FFIR) filter is formulated by the discretization of the minimization problem with the finite element method. For the finite element discretization, the Hermitian shape function is utilized. The proposed FFIR filter is capable of reconstructing displacement and velocity simultaneously. The fundamental characteristics of the proposed filters are investigated in the frequency domain using the transfer and accuracy functions. It is shown that the proposed FIR filters suppress low frequency noise components in measured accelerations effectively, and reconstruct physically meaningful displacement accurately. The validity of the proposed filters is demonstrated through a numerical simulation study, a field experiment and an evaluation of flutter derivatives using measurements taken from a wind tunnel test.

1. Introduction

Dynamic displacement and velocity induced by structure vibration can be utilized for various engineering applications such as structural health monitoring [1], structural control [2] and the evaluation of the dynamic properties of a structure [3]. Although displacement is measurable with various types of modern devices in theory, displacement is very difficult to measure for large-scale structures in real situations because fixed reference points are rarely found [4]. The situation is even worse for the measurement of velocity as virtually no velocity transducers are available. On the other hand, various types of accelerometers are commercially available, and no fixed reference point is required to measure acceleration. Therefore, acceleration is primarily measured in structures rather than displacement or velocity.

A great number of approaches have been proposed to reconstruct displacement from measured accelerations [4–10]. Among them, the digital filters and the frequency domain integration approach (FDIA) are frequently adopted in previous

---

[*] Corresponding author. Tel.: +82 2 880 8388; fax: +82 2 873 2684.
E-mail address: chslee@snu.ac.kr (H.S. Lee).

0022-460X/$ - see front matter © 2010 Elsevier Ltd. All rights reserved.
doi:10.1016/j.jsv.2010.05.016

works. The finite impulse response (FIR) filter [7] and infinite impulse filter (IIR) [5,6,9,10] are well-known digital filters that are applicable to the displacement reconstruction. The IIR filters generally require initial conditions on displacement and/or velocity, which are impossible to prescribe in real situations. Moreover, low-frequency noise components are amplified and propagate through time. Some remedies have been proposed to overcome these drawbacks, but they require additional pieces of information [10] or cause another type of errors such as phase errors [7,9]. The conventional FIR (CFIR) filter reconstructs displacement by the linear combination of measured accelerations. The coefficients of the CFIR filter are determined by approximating a given transfer function in the frequency domain with a truncated Fourier series [5,6]. In case the exact transfer function is employed for the CFIR filter, the coefficients of the Fourier series cannot be evaluated with the standard approach utilizing the normality of the trigonometric functions due to the singularity at the zero frequency [6,7]. Here, the exact transfer function implies the transfer function of the exact governing differential equation between displacement and acceleration.

The FDIA [6] reconstructs displacement by applying the inverse Fourier transform to the Fourier transform of measured accelerations multiplied by the exact transfer function. The FDIA requires a rather large computational effort, and may be inadequate for real-time or near real-time processing because the Fourier transform and the inverse Fourier transform should be performed for every reconstruction step [11]. Moreover, a low-cut filter or a band-pass filter should be introduced to suppress low frequency noise components in measured acceleration when the exact transfer function is employed for the reconstruction.

Lee et al. [11] recently proposed a new type of FIR filter based on the inverse problem discretized by the finite difference method, and demonstrated the accuracy and stability of the FIR filter through numerical and experimental studies. Since, however, they employ the discretized form of the inverse problem for the design of the filter, the governing differential equation of the inverse problem is not derived. Consequently, a CFIR filter based on the transfer function of the inverse problem cannot be formulated, and the exact relationship between the accuracy of the filter and the regularization factor in the inverse problem is not fully recognized. The regularization factor, which governs the accuracy of the filter, is defined empirically rather than analytically as a function of the filter size that affects the stability of the filter, and thus the stability and the accuracy of the filter cannot be adjusted independently. Another limitation of their work is that the reconstruction of velocity is not considered.

This paper proposes two types of FIR filters, the CFIR filter and the FEM-FIR (FFIR) filter based on the inverse problem formulated by Lee et al. [11] for the reconstruction. Unlike their work, however, the continuous form of the minimization problem defining the inverse problem is utilized in this study. The governing equation of the inverse problem is obtained by taking variation of the minimization problem, which leads to the same type of differential equation as that of a beam on an elastic foundation (BEF) [12]. The transfer function of the inverse problem is hereafter referred to as the BEF transfer function. The exact relation between the regularization factor and the accuracy of the proposed filter is established through the desired accuracy at the target frequency, which is the lowest frequency in physically meaningful frequency contents in measured acceleration. Two filter sizes are proposed for the CFIR filter from the viewpoint of the stability independently to the regularization factor. As the BEF transfer function is capable of suppressing noise components below the target frequency, the FDIA without a low-cut filter or a band-pass filter is presented using the BEF transfer function.

The coefficients of the CFIR and the FFIR filter are obtained by approximating the BEF transfer function with the Fourier series in the frequency domain and by discretizing the inverse problem with the standard finite element method in the time domain, respectively. The proposed filters have their own merits and disadvantages in relation to each other. The filter size can be selected arbitrarily for the FFIR filter, while the uniform frequency responses are expected in the CFIR filter for the proposed filter sizes. A great advantage of the FFIR filter over the CFIR filter is that velocity as well as displacement can be reconstructed simultaneously as the velocity field is embedded in the finite element model of the FFIR filter. The characteristics of the proposed FIR filters are presented and discussed in detail by investigating the transfer and accuracy functions [6,10].

Three examples are presented for demonstrating the validity of the proposed filters. Various characteristics of the CFIR and FFIR filters are verified with reconstructed displacement and velocity from numerically simulated accelerations in the first example. Displacement is reconstructed from the accelerations measured in a simply supported railroad bridge during commercial operation, and is compared with the measured displacement in the second example. The third example presents the evaluation of the flutter derivatives [3,13] using the reconstructed displacement, and compares the results with those obtained by measured displacements in a wind tunnel test.

2. Variational statement of an inverse problem

2.1. The exact governing equation and transfer function

Acceleration is defined as the second time derivative of displacement at a fixed material point. In case the acceleration is continuously measured for a time interval $T_1 < t < T_2$, and the displacements at the both ends of the time interval are specified, displacement is reconstructed from the measured acceleration by solving the following boundary value problem:

$$a(t) \equiv \frac{\mathrm{d}^2 u(t)}{\mathrm{d}t^2} \approx \bar{a}(t), \quad T_1 < t < T_2, \quad u(T_1) = \bar{u}_1 \text{ and } u(T_2) = \bar{u}_2 \tag{1}$$

where $u(t)$, $\overline{a}(t)$, $\overline{u}_1$ and $\overline{u}_2$ are the displacement and the measured acceleration, prescribed displacements at $t=T_1$ and $t=T_2$, respectively. A time interval in which displacement is to be reconstructed is hereafter referred to as a time window. As only the dynamic information is utilized for the displacement reconstruction in this paper, the displacement in Eq. (1) represents the dynamic component measured from the static equilibrium position of a structure.

The homogenous solution of Eq. (1) is given as a linear function in time. Since, however, the real dynamic displacement induced by structural vibration is defined with harmonic functions through the Duhamel integral [14], a linear function is not an adequate basis for the dynamic displacement induced by structural vibration. Therefore, the homogeneous solution should vanish, and the solution of Eq. (1) is expressed solely by the particular solution. The displacements at the boundaries of a time window are determined by the particular solution rather than specified as boundary conditions. The particular solution can be found through the Fourier transform. The transfer function of Eq. (1) is derived by the Fourier transform [7]

$$F(u(t)) = H_E(\omega)F(\overline{a}(t)) = -\frac{1}{\omega^2}F(\overline{a}(t)) \tag{2}$$

where F and $H_E=-1/\omega^2$ denote the Fourier transform and the exact transfer function of the differential equation in Eq. (1), respectively, and ω is the angular frequency. The time-history of displacement is obtained by applying the inverse Fourier transform to Eq. (2)

$$u(t) = -F^{-1}\left(\frac{1}{\omega^2}F(\overline{a}(t))\right) \tag{3}$$

where F^{-1} represents the inverse Fourier transform. The displacement reconstruction scheme defined in (3) is referred to as the frequency domain integration approach (FDIA).

In case the measured acceleration contains random noise, pure noise frequency contents in measured accelerations below the target frequency are severely amplified by the exact transfer function in the frequency domain [10]. Consequently, the reconstructed displacement in the time domain is polluted with the amplified noise components. The target frequency is easily determined by investigating the Fourier transform of measured accelerations. Even if measured accelerations are noise-free, the FDIA defined in Eq. (3) cannot be directly applied to reconstruct displacement. Since the Fourier transform of measured accelerations in Eq. (3) is performed on the finite time interval, the Fourier transform contains frequency responses below the target frequency [5,6], which should not exist. This truncation error acts as an additional source of noise, and thus pollutes the reconstructed displacement in the time domain similar to the random measurement noise. To suppress the measurement noise and the truncation error below the target frequency, low cut filters or band pass filters are usually applied to Eq. (3) before performing the inverse Fourier transform

$$u(t) = -F^{-1}\left(\frac{1}{\omega^2}\phi(\omega)F(\overline{a}(t))\right) \tag{4}$$

where ω is the angular frequency, and ϕ is a proper weighting function [6] for a low cut filter or a band pass filter.

2.2. The governing equation and transfer function of an inverse problem

Lee et al. [11] have proposed a new class of displacement reconstruction scheme with measured acceleration based on an inverse problem. In their approach, the displacement is reconstructed by solving the following minimization problem defined in a time window:

$$\operatorname*{Min}_{u} \Pi(u) = \frac{1}{2}\int_{T_1}^{T_2}\left(\frac{\mathrm{d}^2u}{\mathrm{d}t^2}-\overline{a}\right)^2\mathrm{d}t + \frac{\beta^2}{2}\int_{T_1}^{T_2}u^2\,\mathrm{d}t \tag{5}$$

The second term in Eq. (5) is a regularization function employed to overcome the ill-posedness and the rank-deficiency of inverse problems, and β is the regularization factor that adjusts the regularization effect in the displacement reconstruction procedure. Only the discretized form of the regularization function has been presented in the work by Lee et al. [11]. Approximation of the second derivative of displacement with the central difference yields a simple quadratic problem, which is easily solved for unknown displacement. The aforementioned approach results in a type of the FIR filter, which is referred to as the FDM-FIR filter hereafter. Since the whole reconstruction procedures are performed in the time domain, the Fourier transform and the inverse Fourier transform are not required at all. The efficiency and accuracy of the FDM-FIR filter are proven through various examples. Lee et al. [11], however, neither derive the transfer function of the inverse problem defined in Eq. (5) nor relate the regularization factor to the accuracy of the filter.

The governing equation and the boundary conditions associated with the minimization problem is obtained by taking the variation of the object function in Eq. (5)

$$\delta\Pi(u) = \int_{T_1}^{T_2}\frac{\mathrm{d}^2\delta u}{\mathrm{d}t^2}\left(\frac{\mathrm{d}^2u}{\mathrm{d}t^2}-\overline{a}\right)\mathrm{d}t + \beta^2\int_{T_1}^{T_2}\delta u u\,\mathrm{d}t = 0 \tag{6}$$

The integration of the first term of Eq. (6) by parts twice leads to the following equation:

$$\int_{T_1}^{T_2} \delta u\left(\frac{\mathrm{d}^4u}{\mathrm{d}t^4}+\beta^2u-\frac{\mathrm{d}^2\overline{a}}{\mathrm{d}t^2}\right)\mathrm{d}t+\frac{\mathrm{d}\delta u}{\mathrm{d}t}\left(\frac{\mathrm{d}^2u}{\mathrm{d}t^2}-\overline{a}\right)\Bigg|_{T_1}^{T_2}-\delta u\left(\frac{\mathrm{d}^3u}{\mathrm{d}t^3}-\frac{\mathrm{d}\overline{a}}{\mathrm{d}t}\right)\Bigg|_{T_1}^{T_2}=0 \tag{7}$$

Based on the above variational statement, the governing equation and the boundary conditions of the minimization problem are defined as follows:

$$\frac{\mathrm{d}^4u}{\mathrm{d}t^4}+\beta^2u=\frac{\mathrm{d}^2\overline{a}}{\mathrm{d}t^2}\ \ T_1<t<T_2 \text{ and } \frac{\mathrm{d}^2u}{\mathrm{d}t^2}=\overline{a},\quad \frac{\mathrm{d}^3u}{\mathrm{d}t^3}=\frac{\mathrm{d}\overline{a}}{\mathrm{d}t} \text{ at } t=T_1,T_2 \tag{8}$$

Since the displacements and the velocity are unknown at the boundaries, the Neumann type boundary conditions [15] are adopted. The governing equation in Eq. (8) is the same as that of a beam on an elastic foundation (BEF). The existence and uniqueness of the solution can be guaranteed with only the Neumann type boundary conditions by virtue of the second term of the left-hand side of the governing equation, which comes from the regularization function.

The transfer function of the governing equation in Eq. (8), which is abbreviated to the BEF transfer function, is derived by applying the Fourier transform

$$H_B(\omega)=-\frac{\omega^2}{\omega^4+\beta^2}=-\frac{(2\pi f)^2}{(2\pi f)^4+\beta^2} \tag{9}$$

where f is the frequency and H_B denotes the BEF transfer function. The time-history of displacement is reconstructed by the FDIA with the BEF transfer function

$$u(t)=F^{-1}(H_B(\omega)F(\overline{a}(t)))=-F^{-1}\left(\frac{\omega^2}{\omega^4+\beta^2}F(\overline{a}(t))\right) \tag{10}$$

It is not necessary to apply a low-cut filter to the FDIA defined in Eq. (10) as the BEF transfer function by itself is capable of suppressing noise components below the target frequency.

Fundamental characteristics of the transfer function are conveniently investigated by the normalization with respect to the target frequency as proposed by Lee et al. [11]

$$\tilde{H}_B(\tilde{f})=-\frac{H_B(\omega)}{1/(2\pi f_T)^2}=\frac{(2\pi f)^2/(2\pi f_T)^2}{((2\pi f)^4+\beta^2)/(2\pi f_T)^4}=\frac{\tilde{f}^2}{(\tilde{f}^4+\beta^2/(2\pi f_T)^4)} \tag{11}$$

where $\tilde{H}_B$, f_T and $\tilde{f}=f/f_T$ are the normalized BEF transfer function, the target frequency and the dimensionless frequency normalized to the target frequency, respectively. The term "normalized" is hereafter omitted for brevity of explanation, unless otherwise stated. The accuracy of the reconstructed displacement is defined with the accuracy function, which is the ratio of the transfer function used in the displacement reconstruction to the exact transfer function [6,10]. The accuracy function of the BEF transfer function,$H_B^{\mathrm{acc}}(\omega)$, is defined as follows:

$$H_B^{\mathrm{acc}}(\omega)=\frac{H_B}{H_E}=\frac{\omega^4}{\omega^4+\beta^2}=\frac{\tilde{f}^4}{(\tilde{f}^4+\beta^2/(2\pi f_T)^4)} \tag{12}$$

The accuracy function in Eq. (12) becomes 0 at $\tilde{f}=0$, and the accuracy function rapidly converges to 1 as the frequency approaches to the target frequency. The transition characteristics of the BEF transfer function in $0\le\tilde{f}\le 1$ are governed by the magnitude of the regularization factor. The accuracy at the target frequency is obtained by setting $\tilde{f}=1$ in Eq. (12)

$$\alpha_T=\frac{1}{1+\beta^2/(2\pi f_T)^4} \tag{13}$$

where α_T is the target accuracy, i.e., the desired accuracy for the reconstructed displacement. If the target accuracy is preselected based on an engineering sense, the regularization factor is determined by the following equation:

$$\beta=\sqrt{\frac{1-\alpha_T}{\alpha_T}}(2\pi f_T)^2=\lambda^2(\alpha_T)(2\pi f_T)^2\ \ 0\le\alpha_T\le 1 \tag{14}$$

where $\lambda^4(\alpha_T)=(1-\alpha_T)/\alpha_T$. Substitution of Eq. (14) into Eqs. (11) and (12) leads to the following expressions:

$$\tilde{H}_B(\tilde{f})=\frac{\tilde{f}^2}{\tilde{f}^4+\lambda^4(\alpha_T)} \tag{15}$$

$$H_B^{\mathrm{acc}}(\tilde{f})=\frac{\tilde{f}^4}{\tilde{f}^4+\lambda^4(\alpha_T)} \tag{16}$$

The BEF transfer functions and the accuracy functions for various levels of target accuracy are drawn in Figs. 1 and 2, respectively, along with the exact transfer function. The BEF transfer function begins to decrease quickly below the target

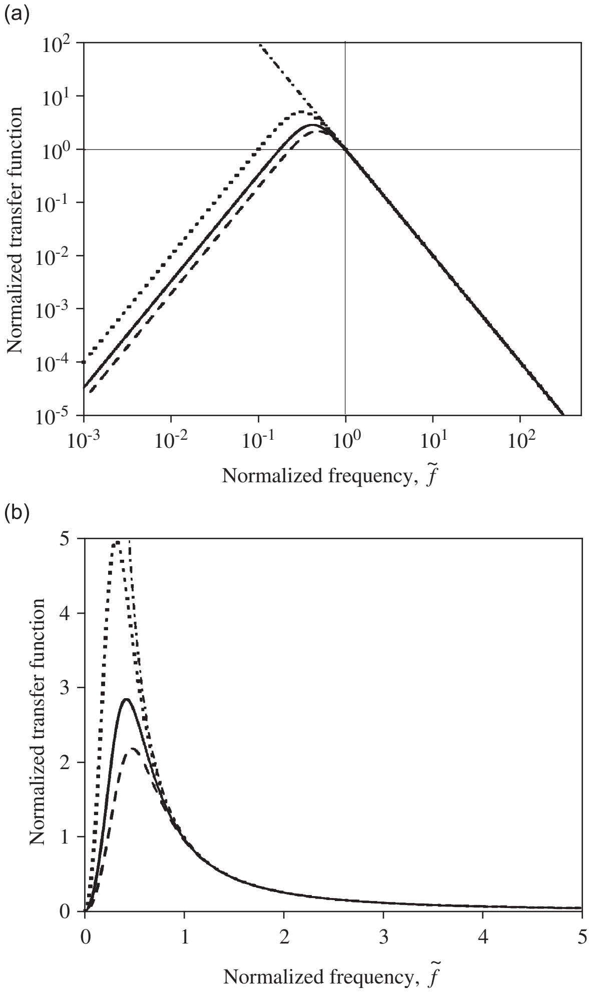

Fig. 1. BEF transfer functions for various levels of the target accuracy: (a) log–log scale and (b) detail in a linear scale. (– –) α_T=0.95; (——) α_T=0.97; (- - - - -) α_T=0.99; and (- - - –) exact transfer function.

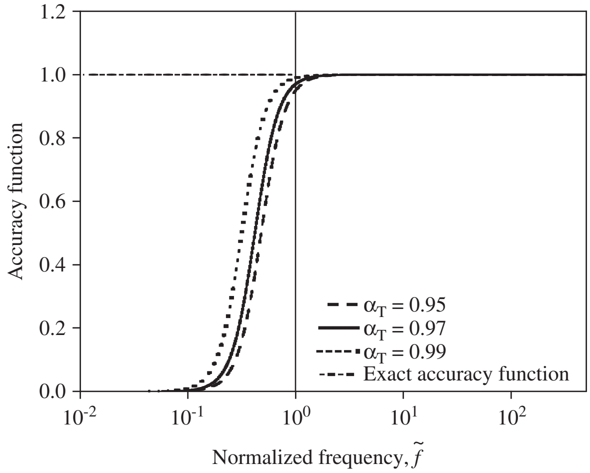

Fig. 2. Accuracy functions for various levels of the target accuracy.

frequency while the exact transfer function keeps increasing as the frequency approaches to zero. For frequency ranges larger than the target frequency, the BEF transfer function and the exact transfer function are almost identical regardless of the target accuracy. Therefore, the FDIA with the BEF transfer function is able to reconstruct the displacement components for $\tilde{f} \geq 1$. Meanwhile, the BEF transfer function suppresses the acceleration components below the target frequency, which are merely measurement noises, in the displacement reconstruction. The degree of the noise suppression becomes stronger as the frequency approaches zero. Higher target accuracy yields weaker noise-suppression capability of the BEF transfer function, and vice versa as shown in Fig. 2. As an apparent trade-off between the accuracy and the noise-suppression exists in the selection of the target accuracy, the optimal target accuracy depends on a specific problem. For example, in case the noise level of measured accelerations is expected to be high, lower target accuracy may be adequate to provide strong noise suppression capability to the BEF transfer function. The target accuracy of 0.97 is selected for all forthcoming discussions in this study.

3. Design of FIR filters and accuracy analysis

3.1. Conventional FIR filter

A conventional finite impulse response (CFIR) filter approximates a given transfer function in the frequency domain. A CFIR filter based on the BEF transfer function is designed in this section. Fig. 3 illustrates the basic setups for the formulation of the CFIR filter. In case accelerations are measured discretely by a uniform time increment, Δt, the CFIR filter expresses the displacement at the center of the time interval, u_{k+1}, as a linear combination of measured accelerations in a time window

$$u_{k+1} = u(t) = (\Delta t)^2 \sum_{p=1}^{2k+1} c_p \bar{a}_p = (\Delta t)^2 \sum_{p=-k}^{k} c_{p+k+1} \bar{a}(t+p\Delta t) \tag{17}$$

Here, c_p is the coefficient of the CFIR filter. It is assumed that a time window contains $2k+1$ measured acceleration and that u_{k+1} represents the reconstructed displacement at time t. The square of the time increment is introduced in Eq. (17) to make the coefficients of the CFIR filter dimensionless. The size of the time window is referred to as the filter size. Once the displacement is computed for time t, the time window moves forward by Δt to reconstruct the displacement at $t+\Delta t$. This procedure is identical to the overlapping time-window technique proposed by Park et al. [16] for the structural damage detection.

The Fourier transform of Eq. (17) yields the transfer function of the CFIR filter [11]

$$H_C(f) = (\Delta t)^2 \sum_{p=-k}^{k} c_{p+k+1} \mathrm{e}^{\mathrm{i}2\pi f p \Delta t} \tag{18}$$

where $H_C(f)$ is the transfer function of the CFIR filter, and i is the imaginary unit. The transfer function of the CFIR filter is supposed to approximate the BEF transfer function given in Eq. (9)

$$H_B(f) \approx (\Delta t)^2 \sum_{p=-k}^{k} c_{p+k+1} \mathrm{e}^{\mathrm{i}2\pi f p \Delta t} \tag{19}$$

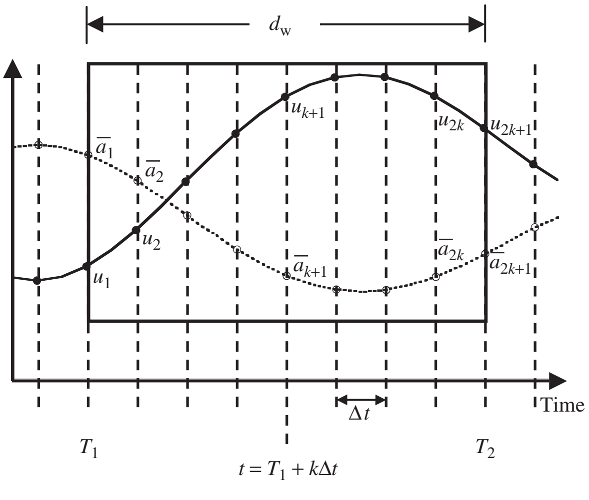

Fig. 3. A time window and measured accelerations for FIR filters.

Eq. (19) represents the truncated Fourier series of the BEF transfer function, and the coefficients of the CFIR filter are determined as follows:

$$c_{p+k+1}=\frac{1}{\Delta t}\int_{-f_s/2}^{f_s/2}H_{\mathrm{B}}(f)\mathrm{e}^{\mathrm{i}2\pi f\,\Delta tp}\mathrm{d}f=-\frac{1}{\Delta t}\frac{1}{(2\pi)^2}\int_{-f_s/2}^{f_s/2}\frac{f^2}{f^4+\lambda^4 f_T^4}\cos(2\pi pf\,\Delta t)\,\mathrm{d}f=-\frac{1}{2\pi^2\tilde{f}_T}\int_0^{1/(2\tilde{f}_T)}\frac{\tilde{f}^2}{\tilde{f}^4+\lambda^4}\cos(2\pi p\tilde{f}_T\tilde{f})\,\mathrm{d}\tilde{f} \quad (20)$$

where $f_s=1/\Delta t$ and $\tilde{f}_T=f_T/f_s$ denote the sampling frequency of measurement and the target frequency to the sampling frequency (TSF) ratio, respectively. The coefficient of the CFIR filter approximating the exact transfer function cannot be evaluated like Eq. (20) due to the singularity at the zero frequency.

The coefficients in Eq. (20) are always real and symmetric with respect to $p=0$ since the BEF transfer function is an even function in the frequency domain. As the BEF transfer function decreases rapidly for larger $\tilde{f}$ as shown in Fig. 1(b), the integral in Eq. (20) is nearly independent of the upper limit for a small TSF ratio of $\tilde{f}_T\leq 0.1$, and thus becomes a function of $\tilde{p}=p\tilde{f}_T$. Consequently, the relation between $\tilde{c}_{p+k+1}=c_{p+k+1}\tilde{f}_T$ and $\tilde{p}$ is TSF ratio independent as shown in Fig. 4(a). The trapezoidal rule is employed to evaluate the integral. Although the number of terms included in the CFIR filter varies with filter sizes, the coefficients for the same p are always identical for all filter sizes at a fixed TSF ratio.

The Gibbs phenomenon, which is the rippling characteristics of a truncated Fourier series, occurs in the CFIR transfer function. To reduce the rippling amplitude, the filter size should be selected so that the coefficients smoothly converge to zero as p approaches to k [5,6]. Therefore, the last term of the CFIR filter should correspond to zero-crossing points, $\tilde{p}_0$

$$k\tilde{f}_T=\tilde{p}_0 \text{ or } k=\frac{\tilde{p}_0}{\tilde{f}_T} \quad (21)$$

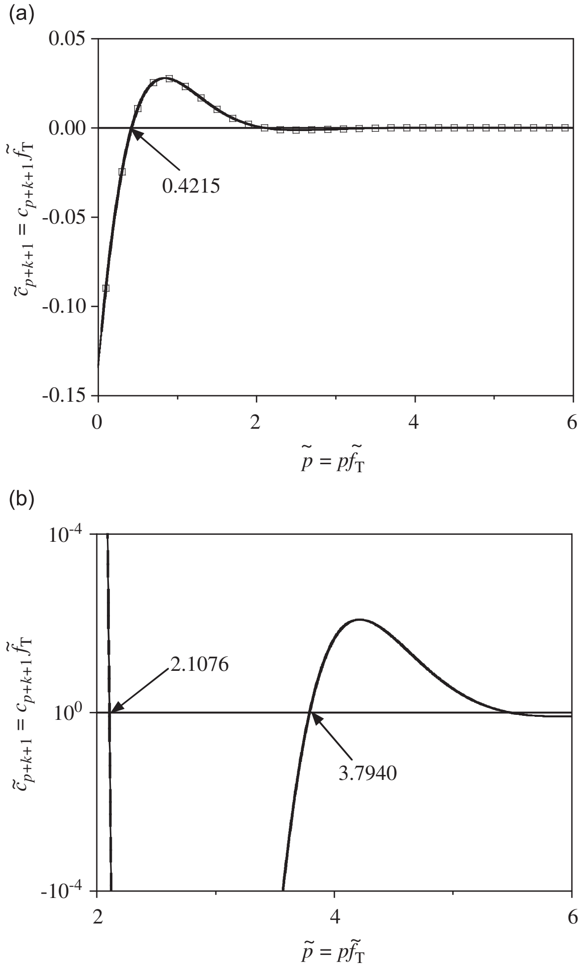

Fig. 4. Coefficients of the CFIR filters for two different TSF ratios: (a) small scale and (b) detail in a large scale. (——) $\tilde{f}_T=1/1000$ and (□) $\tilde{f}_T=100/1000$.

When the calculated value for k with Eq. (21) is not an integer, the closest integer to the calculated k is employed. The filter size is defined using k in Eq. (21)

$$d_w = 2k\Delta t = 2\frac{f_s}{f_T}\tilde{p}_0\Delta t = \frac{2\tilde{p}_0}{f_T} = N_w\frac{1}{f_T} \tag{22}$$

where d_w and $N_w = 2\tilde{p}_0$ are the filter size expressed in terms of time and the target period, respectively. The target period denotes the reciprocal of the target frequency.

The zero-crossing points appear periodically by an interval of 1.687 such as 0.421, 2.108, 3.794, etc., in Fig. 4(b). The filter sizes corresponding to the three zero crossing points become 0.842, 4.215 and 7.588 times the target period. As the coefficient of the CFIR filter does not converge to zero near the first zero-crossing point, the filter size of N_w=0.842 yields a large rippling amplitude in the transfer function (*vide* the forthcoming discussions), and is not an adequate size. The filter sizes of N_w=4.215 and 7.588 result in the acceptable rippling amplitudes in the accuracy functions, and therefore are selected as the standard filter size and the long filter size, respectively. The long filter size yields smaller rippling amplitude but requires more computational effort than the standard one. The selection of the filter size between the standard and long filter size depends on specific applications. Of course, a filter size longer than the long filter size may be utilized, but it is believed that the long filter size gives sufficiently accurate results in an engineering sense.

Because of the symmetry of the coefficients, the transfer function of the proposed CFIR filter becomes as follows:

$$H_C(f) = (\Delta t)^2\left(c_{k+1} + 2\sum_{p=1}^{k} c_{p+k+1}\cos(2\pi pf\Delta t)\right) \tag{23}$$

Since the transfer function of Eq. (23) is always real, the proposed CFIR filer generates no phase error in the reconstructed displacement. The normalized transfer function and accuracy function of the CFIR filter are derived as in the previous section

$$\tilde{H}_C(\tilde{f}) = -(2\pi\tilde{f}_T)^2\left(c_{k+1} + 2\sum_{p=1}^{k} c_{k+1+p}\cos(2\pi p\tilde{f}_T\tilde{f})\right) \tag{24}$$

$$H_C^{\mathrm{acc}}(\tilde{f}) = -(2\pi\tilde{f}_T\tilde{f})^2\left(c_{k+1} + 2\sum_{p=1}^{k} c_{k+1+p}\cos(2\pi p\tilde{f}_T\tilde{f})\right) \tag{25}$$

where $\tilde{H}_C$ and H_C^{acc} are the normalized transfer function and accuracy function of the CFIR filter, respectively.

The transfer function and accuracy function are shown in Figs. 5 and 6, respectively, for the standard and long filter sizes at the TSF ratio of 1/1000. The CFIR filters for both the filter sizes approximate the BEF transfer function very well for $\tilde{f} \geq 1$. The transfer function for N_w=5 oscillates severely, and tends to diverge as the frequency increases. The oscillations in the transfer function are always observed for filter sizes other than the standard and long filter sizes. The smaller filter size except the two filter sizes not only causes the larger oscillation amplitude, but also triggers the oscillation at the smaller frequency. The transfer function of the CFIR filter with the standard filter size decreases faster than that with the long filter size for $\tilde{f} \leq 0.1$, and becomes negative when $\tilde{f} \leq 0.043$ (Fig. 5(b)). The negative transfer function causes the phase error of π in the reconstructed displacement. Since, however, only noise components exist in the frequency range, the negative transfer function would not cause any phase error for physically meaningful displacement components. As shown in Fig. 5(b), the transfer functions for the standard and long filter sizes converge to –0.079 and 0.004 at $\tilde{f} = 0$, respectively. This fact implies that the long filter size provides stronger noise suppression capability in the extremely low frequency range than the standard filter size to the CFIR filter.

The Gibbs phenomenon is clearly observed in the plot of the accuracy function in Fig. 6. The rippling amplitudes for the standard and long filter sizes are 1.4% and 0.06%, respectively. The rippling of the accuracy function is hardly noticeable for the long filter size even in the large scale plot shown in Fig. 6(b). The accuracy functions for the standard filter size at two different TSF ratios of 1/1000 and 10/1000 are presented in Fig. 7, and are almost identical up to the corresponding Nyquist frequencies. The enlarged plot of the accuracy functions near the target frequency is also presented in Fig. 7(b). The rippling amplitude of the accuracy function for the TSF ratio of 10/1000 increases slightly near the Nyquist frequency. The accuracy at the target frequency is evaluated as 0.984 for the both TSF ratios.

The proposed CFIR filter exhibits uniform frequency responses from the target frequency to the Nyquist frequency, and is able to reconstruct displacement with the same level of accuracy independent of the TSF ratio for the frequency range. Noise components below the target frequency are effectively suppressed in the CFIR filter. The only restriction of the proposed CFIR filter is that the filter size should be fixed at either the standard or long filter size, and cannot be adjusted freely as needed in actual applications.

3.2. *FEM-FIR filter*

The direct discretization of the variation statement in Eq. (6) with the finite element method leads to a new class of FIR filter, which is referred to as the FEM-FIR filter (FFIR filter). The FFIR filter is formulated purely in the time domain unlike the other reconstruction schemes presented in this study, and is able to reconstruct displacement and velocity at the same

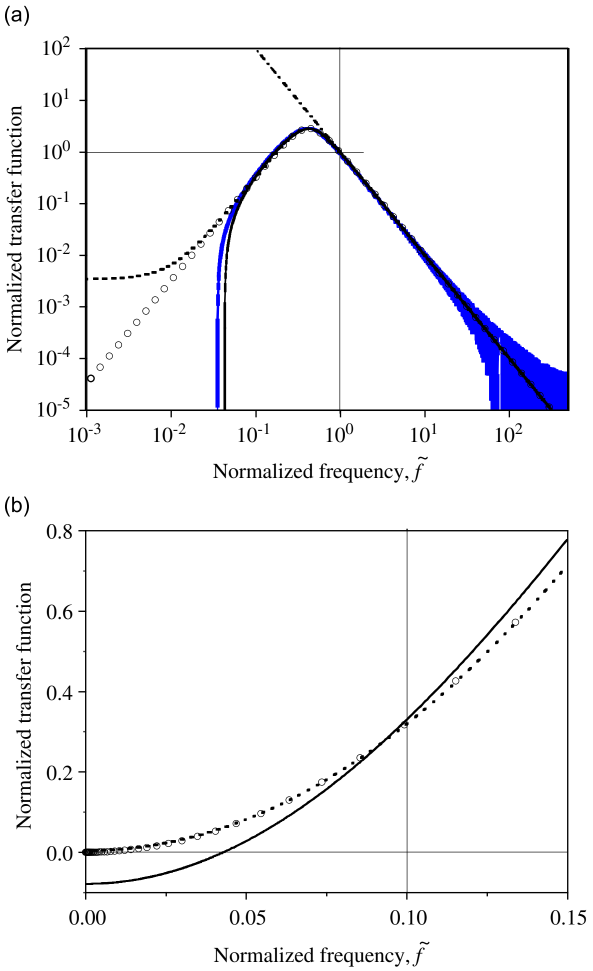

Fig. 5. Transfer functions for the CFIR filters for various filter sizes: (a) log–log scale and (b) detail in a linear scale. (——) N_w=4.215; (▬) N_w=5.000; (- - - - -) N_w=7.588; (○) BEF transfer function; and (- - - -) exact transfer function.

time. A similar approach (FDM-FIR filter) has been proposed by Lee et al. [11] using the FDM to discretize Eq. (5), but the reconstruction of velocity is not considered. The filter size of the FDM-FIR filter is proposed empirically without proper considerations of the rippling amplitude, and the regularization factor is determined by the filter size. As discussed previously, the regularization factor and the filter size govern the accuracy and stability of the filter, respectively, which are two independent aspects of a numerical method. However, the accuracy and stability of the FDM-FIR filter cannot be independently controlled because the regularization factor is defined as a function of the filter size.

As the CFIR filter, the FFIR filter reconstructs displacement and velocity using the moving time-window technique. The standard and long filter sizes defined for the CFIR filter in the previous section are adopted for the FFIR filter. Eq. (6) is discretized in time with $2k$ elements representing the time increments

$$\delta\Pi(u)=\sum_{e=1}^{2k}\int_{\Delta t}\frac{\mathrm{d}^2\delta u^e}{\mathrm{d}t^2}\left(\frac{\mathrm{d}^2u^e}{\mathrm{d}t^2}-\overline{a}^e\right)\mathrm{d}t+\beta^2\sum_{e=1}^{2k}\int_{\Delta t}\delta u^e u^e\,\mathrm{d}t=0 \tag{26}$$

Here, u^e and $\overline{a}^e$ denote the displacement and acceleration in element, e, respectively. The displacement is interpolated with the Hermitian shape function, $\mathbf{N}_H$, and the measured acceleration is interpolated with the linear shape function, $\mathbf{N}_L$, in an element [17]

$$u^e=\mathbf{N}_H\cdot\mathbf{u}^e,\quad \overline{a}^e=\mathbf{N}_L\cdot\overline{\mathbf{a}}^e \tag{27}$$

where $\mathbf{u}^e$ and $\overline{\mathbf{a}}^e$ are the nodal unknown vector and measured nodal acceleration in element e, respectively, and are defined as follows:

$$\mathbf{u}^e=(u_1^e,v_1^e,u_2^e,v_2^e)^{\mathrm{T}},\quad \overline{\mathbf{a}}^e=(\overline{a}_1^e,\overline{a}_2^e)^{\mathrm{T}} \tag{28}$$

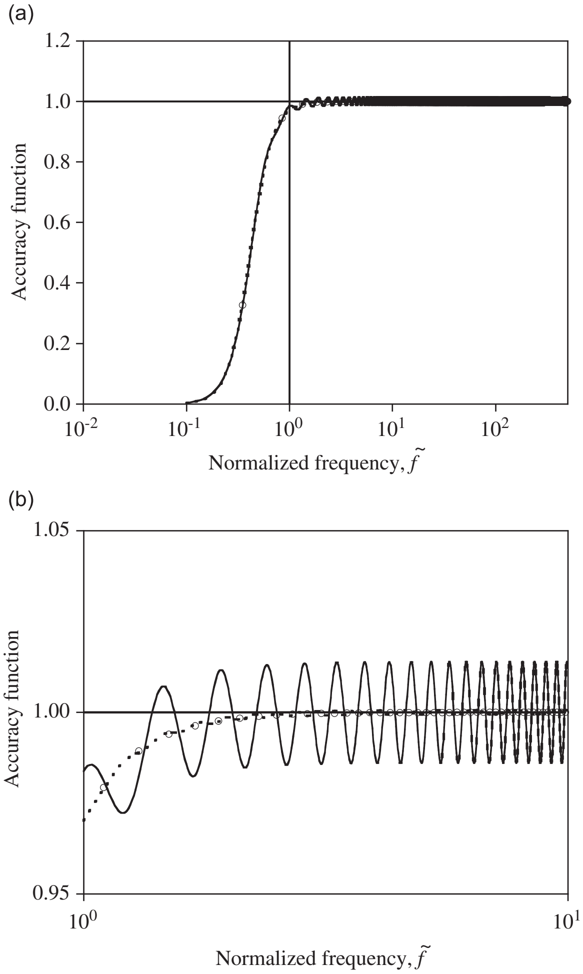

Fig. 6. Accuracy functions of the CFIR filter for the standard and the long filter sizes: (a) small scale and (b) detail in a large scale. (——) N_w=4.215; (- - - - -) N_w=7.588; and (○) BEF transfer function.

where $(\cdot)_1^e$ and $(\cdot)_2^e$ indicate nodal unknowns at the left and the right node of element e, respectively, and v is the velocity. The definitions of the nodal variables are illustrated in Fig. 8. Notice that the measured acceleration may be modeled as a constant in an element by averaging the two nodal accelerations if necessary.

The standard FEM formulation for a beam on an elastic foundation [12] is adopted to derive the following matrix expression of Eq. (26):

$$(\mathbf{K}+\beta^2(\Delta t)^4\mathbf{M})\mathbf{u}=(\Delta t)^2\mathbf{Q}\bar{\mathbf{a}} \tag{29}$$

where $\mathbf{u}$ and $\bar{\mathbf{a}}$ denote the nodal unknown vector and the measured acceleration vector associated with all sampling points of measurement. The nodal unknown vector consists of the nodal displacements and the nodal velocities. The matrices in Eq. (29) are defined as

$$\mathbf{K}=\sum_e\int_0^1\frac{\mathrm{d}^2\mathbf{N}_H^T}{\mathrm{d}\xi^2}\frac{\mathrm{d}^2\mathbf{N}_H}{\mathrm{d}\xi^2}\,\mathrm{d}\xi,\quad \mathbf{M}=\sum_e\int_0^1\mathbf{N}_H^T\mathbf{N}_H\,\mathrm{d}\xi,\quad \mathbf{Q}=\sum_e\int_0^1\frac{\mathrm{d}^2\mathbf{N}_H^T}{\mathrm{d}\xi^2}\mathbf{N}_L\,\mathrm{d}\xi \tag{30}$$

where $\sum_e$ is the assembly operator of the FEM, and ξ is the natural coordinate [17] for the time variable ranging from 0 to 1. The nodal unknown vector is obtained by solving Eq. (29).

$$\mathbf{u}=(\Delta t)^2(\mathbf{K}+\beta^2(\Delta t)^4\mathbf{M})^{-1}\mathbf{Q}\bar{\mathbf{a}}=(\Delta t)^2\mathbf{C}\bar{\mathbf{a}} \tag{31}$$

where $\mathbf{C}$ is the coefficient matrix of order $2(2k+1)\times(2k+1)$.

Since the Neumann type boundary conditions are enforced in a weak sense for Eq. (29), the reconstructed variables are inevitably affected by errors in the boundary conditions. However, the errors rapidly decrease inside of the domain away from the boundary due to the diffusive characteristics of the FEM for elliptic boundary value problems. The displacement

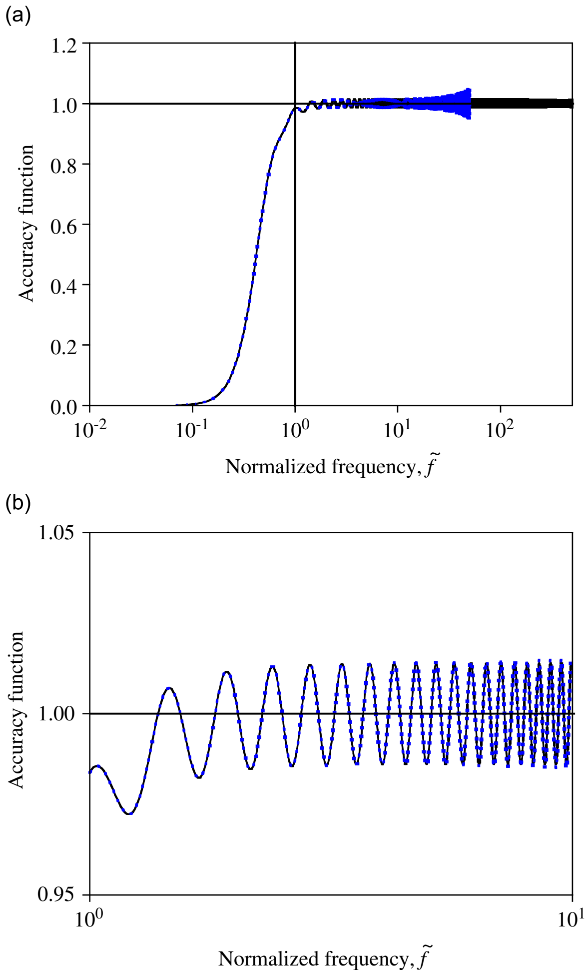

Fig. 7. Accuracy functions of the CFIR filter for two different TSF ratios: (a) small scale and (b) detail in a large scale. (——) $\tilde{f}_T = 1/1000$ and (▪ ▪ ▪ ▪ ▪) $\tilde{f}_T = 10/1000$.

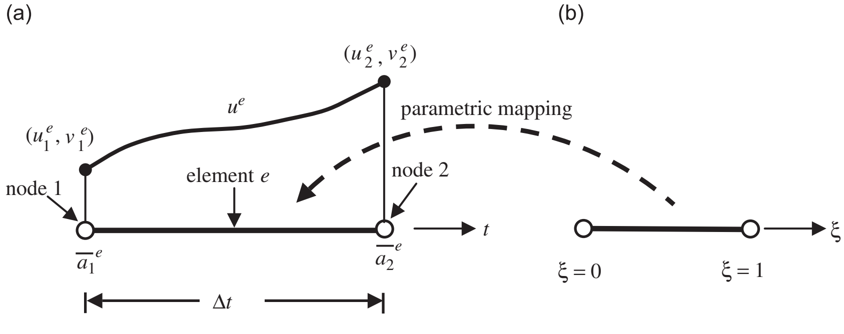

Fig. 8. Finite element model for the FFIR filter.

and velocity at the center of a time window are least affected by the errors induced by the weak enforcement of the boundary conditions, and are taken as the reconstructed solution in a time window. Assuming the time step at the center of a time window represents time t as in the CFIR filter, the reconstructed displacement is expressed as

$$u(t) = u_{k+1} = \mathbf{c}\bar{\mathbf{a}}(\Delta t)^2 = (\Delta t)^2 \sum_{p=1}^{2k+1} C_{2k+1,p}\bar{a}_p = (\Delta t)^2 \sum_{p=-k}^{k} c_{p+k+1}\bar{a}(t+p\Delta t) \tag{32}$$

where **c** denotes the $(2k+1)$th row of the **C** matrix. The FFIR and CFIR filters have the identical expression. The only difference between the two filters is the method for determining the coefficients. The transfer function and accuracy function of the FFIR filter in Eq. (32) are derived and normalized with the same method used in the CFIR filter, and are not presented here.

The coefficients of the FFIR filter, c_{p+k+1}, for various window sizes are plotted against p/k for the TSF ratio of 1/1000 in Fig. 9 together with those of the CFIR filter with the standard and long filter size. The coefficients are symmetric with respect to $p=0$ and converge smoothly to zero regardless of filter sizes dissimilar to the CFIR filter. Therefore, as far as the rippling amplitude in the transfer function is concerned, the filter size can be selected freely as needed in specific problems. The convergence to zero becomes smoother for a longer filter size, which yields the smaller rippling amplitude [5,6]. The imaginary parts of the displacement transfer function vanish due to the symmetry of the coefficients, and thus no phase error occurs in the reconstructed displacement with the FFIR filter. The coefficients of the FFIR and the CFIR filter appear to be almost identical in the figure, and the differences in the coefficients between the two filters seem negligible. However, the differences cause considerable effect on behaviors of the two filters.

The displacement transfer functions of the FFIR filters with various filter sizes for the TSF ratio of 1/1000 are presented in Fig. 10. The transfer functions appear almost identical above the target frequency regardless of the filter size in the figure, but the longer filter size provides stronger noise suppression capability for the FFIR filter. The transfer function of the FFIR filter approximates the BEF transfer function better than that of the CFIR filter shown in Fig. 5 below the target frequency for the same filter size. The severe oscillations in the transfer function of the CFIR filter found for $N_w=5$ do not occur in the FFIR at all. The Gibbs phenomenon is clearly seen in the accuracy functions plotted for various filter sizes in Fig. 11. The larger filter size yields the smaller rippling amplitude of the accuracy function, and virtually no rippling in the accuracy function is observed for filter sizes larger than $N_w=5$ as shown in Fig. 11(b). Unlike the CFIR filter, the rippling

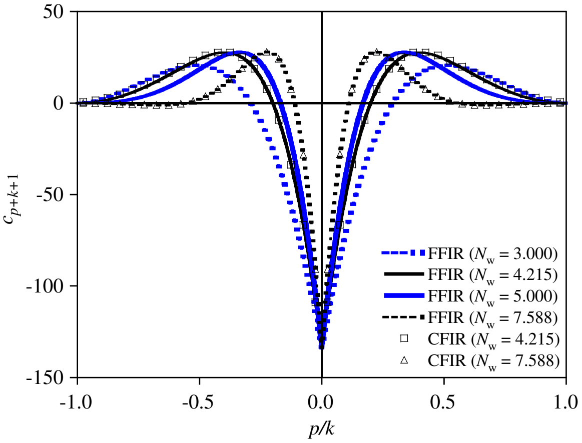

Fig. 9. Coefficients of the FFIR filter for various filter sizes.

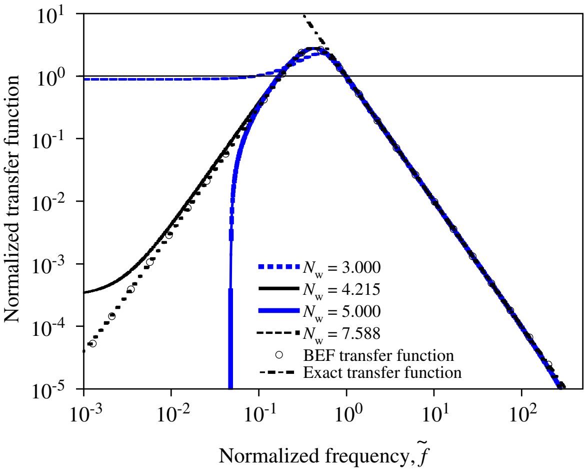

Fig. 10. Transfer functions of the FFIR filter for various filter sizes.

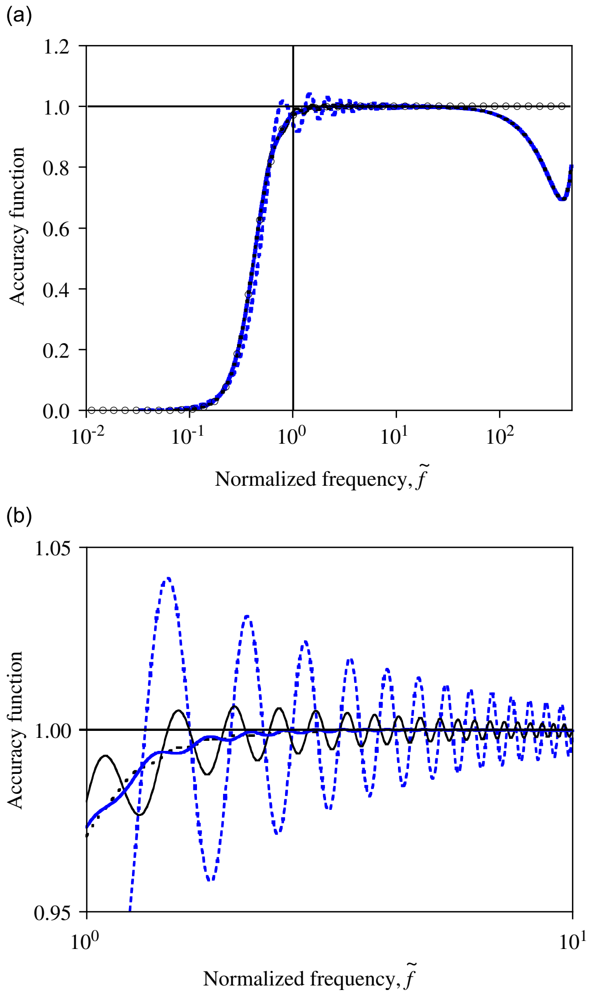

Fig. 11. Accuracy functions of the FFIR filter for various filter sizes: (a) small scale and (b) detail in a large scale: (▪ ▪ ▪ ▪ ▪) N_w=3.000; (——) N_w=4.215; (▬▬▬) N_w=5.000; (- - - - -) N_w=7.588; and (○) BEF transfer function.

amplitude damps out quickly for all filter sizes as the frequency increases. The accuracy at the target frequency varies slightly with the filter size, which is caused by the rippling of the accuracy function. The standard and long filter sizes yield an accuracy of 0.98 and 0.97 at the target frequency, respectively.

Fig. 12(a) presents the accuracy functions of the FFIR filters with the standard filter size for two different TSF ratios of 1/1000 and 10/1000 against the normalized frequency. The accuracy functions plotted against the frequency normalized to the sampling frequency are also presented in Fig. 12(b). The FFIR filter yields identical accuracy functions independent of the TSF ratios near the target frequency. Fig. 12(b) reveals that the accuracy functions begin to deviate from the exact value 1 at 4% of the sampling rate, and become smaller than the target accuracy of 0.97 after 9.7% of the sampling rate regardless of TSF ratios. The FFIR filter yields less accurate transfer functions for high frequencies over $0.1f_s$ than for frequencies near the target frequency. Nevertheless, overall accuracy of the reconstructed displacement would not deteriorate much due to the aforementioned inaccuracy because the transfer function decreases rapidly in proportion to $1/\tilde{f}^2$, and the contribution of high frequency contents in measured acceleration to the reconstructed displacement becomes negligible. To ensure the accuracy of the reconstructed displacement, all dominant frequencies in measured accelerations should be smaller than $0.1f_s$. The frequency range to achieve the accuracy level of 0.97 is given as $f_T \leq f \leq 0.1f_s$.

The accuracy functions of the CFIR and the FFIR filter are compared with that of the FDM-FIR filter proposed by Lee et al. [11] in Fig. 13 at the TSF ratio of 1/1000. As the filter size governs the regularization factor in the original formulation of the FDM-FIR filter, the original formulation is modified with the regularization factor defined in Eq. (14) and the standard filter size for a fair comparison. The accuracy functions of the FDM-FIR and the FFIR filter appear almost identical up to $\tilde{f} = 40$, at which the accuracy functions begin to deviate from 1 to opposite directions. The accuracy function of the FDM-FIR filter reaches 2.46 at the Nyquist frequency, and that of the FFIR filter reaches the minimum value of 0.693 at $\tilde{f} = 390$.

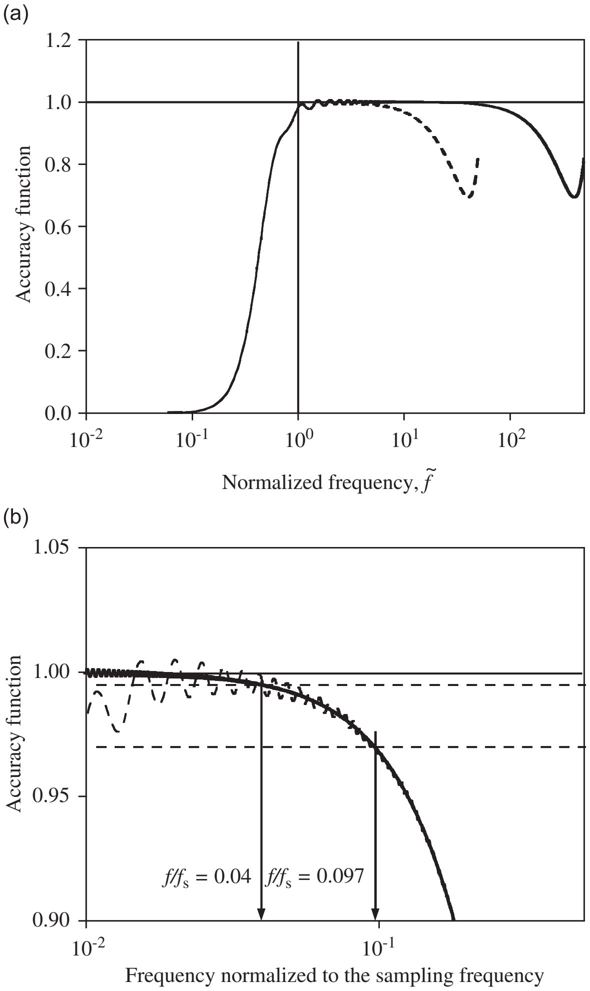

Fig. 12. Accuracy functions of the FFIR filter with the standard filter size for two different TSF ratios: (a) against the normalized frequency and (b) against the frequency normalized to the sampling frequency. (▬) $\tilde{f}_T = 1/1000$ and (– –) $\tilde{f}_T = 10/1000$.

The velocity at the center of a time window is reconstructed using the (2k+2)th row of the coefficient matrix in Eq. (31)

$$v(t) = v_{k+1} = (\Delta t)^2 \sum_{p=1}^{2k+1} C_{2k+2,p}\bar{a}_p = \Delta t \sum_{p=-k}^{k} \hat{c}_{p+k+1}\bar{a}(t+p\Delta t) = \hat{\mathbf{c}}\bar{\mathbf{a}}\Delta t \tag{33}$$

where $\hat{c}_{p+k+1} = \Delta t C_{2k+2,p+k+1}$. The coefficients for the velocity reconstruction are shown in Fig. 14 for various filter sizes at the TSF ratio of 1/1000, and always maintain anti-symmetry with respect to p=0. The anti-symmetry of the coefficients is also held for different TSF ratios because the compositions of the system matrices in Eq. (30) are independent of the TSF ratios. The velocity transfer function of the FFIR filter is obtained by applying the Fourier transformation of Eq. (33). All real parts of the velocity transfer function vanish due to the anti-symmetry of the coefficients

$$V_F(f) = 2\mathrm{i}\Delta t \sum_{p=1}^{k} \hat{c}_{p+k+1}\sin(2\pi p f \Delta t) \tag{34}$$

where V_F is the velocity transfer function of the FFIR. As the exact transfer function for velocity is $1/\mathrm{i}\omega$, the normalized transfer function $\tilde{V}_F$ and the accuracy function V_F^{acc} of velocity are defined as follows:

$$\tilde{V}_F(f) = \frac{V_F(f)}{1/\mathrm{i}\omega_T} = -4\pi\tilde{f}_T \sum_{p=1}^{k} \hat{c}_{p+k+1}\sin(2\pi p\tilde{f}_T\tilde{f}) \tag{35}$$

$$V_F^{\mathrm{acc}}(f) = \frac{V_F(f)}{1/\mathrm{i}\omega} = -4\pi\tilde{f}_T\tilde{f} \sum_{p=1}^{k} \hat{c}_{p+k+1}\sin(2\pi p\tilde{f}_T\tilde{f}) \tag{36}$$

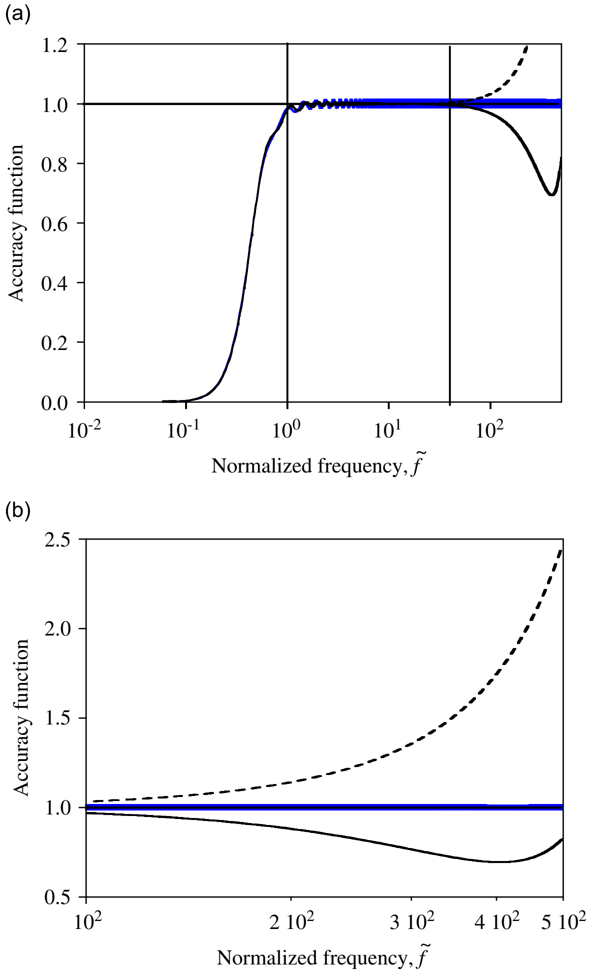

Fig. 13. Accuracy functions of three types of the FIR filters with the standard filter size for the TSF ratio of 1/1000: (a) small scale and (b) detail in a large scale. (━━━━) CFIR filter; (——) FFIR filter and (– –) FDM-FIR filter.

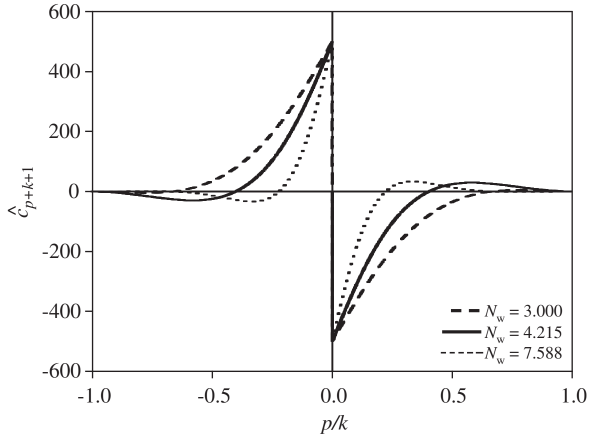

Fig. 14. Coefficients of the velocity FFIR filter for various filter sizes.

The accuracy function of velocity is presented in Fig. 15 for two TSF ratios. As in the displacement reconstruction, most of the frequency contents smaller than the target frequency in measured accelerations are suppressed in the velocity reconstruction. The accuracy of the velocity reconstruction reaches 0.982 at the target frequency, and 0.97 at $0.1f_s$. The accuracy decreases rapidly after $0.1f_s$, and becomes zero at the Nyquist frequency.

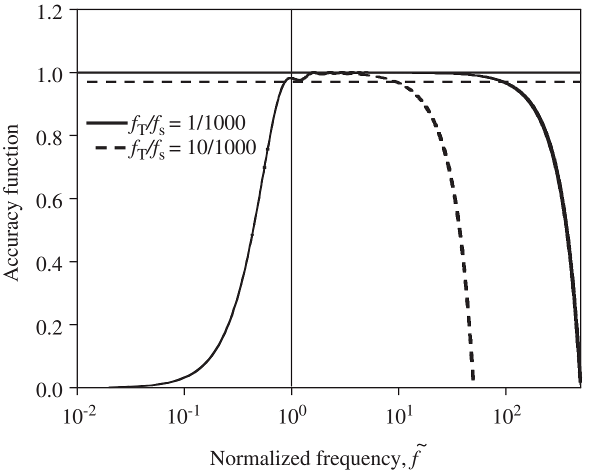

Fig. 15. Velocity accuracy functions of the FFIR filter for various TSF ratios.

An advantage of the FFIR filter over the CFIR filter is that the filter size can be flexibly selected as needed in actual applications. For example, a filter size shorter than the standard filter size may be employed to reduce computational effort for the real-time or near real-time reconstruction of displacement and/or velocity. However, shorter filter sizes lead to a less accurate transfer function at the target frequency and a larger rippling magnitude of the accuracy function. To enhance the accuracy of the FFIR filter for a shorter filter size than the standard size, the two algorithms proposed by the Lee et al. [11] may be adopted. The first approach is applicable when measured acceleration contains only one dominant frequency, and the target frequency is simply adjusted so that the accuracy at the actual target frequency becomes exactly 1. The second approach is appropriate for the measurement with multiple frequency contents, and is based on a minimization problem with respect to the target frequency. For details, refer to Ref. [11].

4. Numerical and experimental verification

Three examples are presented to verify the accuracy and effectiveness of the proposed FIR filters. The first two examples are adopted from the work by Lee et al. [11] on the displacement reconstruction with the FDM-FIR filter. The flutter derivatives are evaluated for a section model of a bridge using the reconstructed displacement from the measured acceleration in the third example. The target accuracy of 0.97 is used for all examples. The reconstruction of displacement and velocity is performed after the actual measurement of the acceleration. Both acceleration and displacement are measured. The instance when the displacement reconstruction begins is set to $t=0$ throughout all the examples. The fast Fourier transform (FFT) is utilized for the discrete Fourier transform. The results by the FDIA based on the BEF transfer function are not presented as the behaviors of the FDIA are not primary concern of this paper. The FDIA yields slightly less accurate results than the proposed filters with the standard filter size and nearly the same results as those with the long filter size.

4.1. Numerical simulation study

The accelerations at the center of a simple beam with the span length of 40 m are measured. The excitation force is applied at the location 12 m right of the left support of the beam, and is defined as follows:

$$\Phi(t) = 8.9\sin 15.4\pi t + 35.9\sin 31\pi t + 29.3\sin 56\pi t KN \tag{37}$$

The flexural rigidity and the mass per unit length of the beam are 6.03×10^{10} N m^2 and 1.5×10^3 kg/m, respectively. The fundamental frequency of the beam is found as 6.22 Hz, and the frequencies of the excitation force are 7.70, 15.50 and 28.00 Hz. The excitation force is withdrawn after 6 s to induce the free vibration of the beam. The dynamic responses of the beam are calculated by the finite element method with 10 beam elements. The Newmark β-method with the constant acceleration assumption is adopted for the time integration in the analysis, and the time increment for the analysis is 0.001 s. The sampling frequency for the measurement of acceleration and displacement is 1000 Hz. The Rayleigh damping model is utilized for structural damping. The first and the second modal damping ratios of 0.1% are assumed to evaluate the coefficients of the Rayleigh damping model. Four dominant frequencies are found as 6.17, 7.67, 15.5 and 28.0 Hz by the FFT on the accelerations calculated for 12 s. The differences between the identified and actual dominant frequencies are caused by the discretization error in the FFT. The ratios of the amplitudes of the simulated displacement components corresponding to the second, the third and the fourth dominant frequencies to that corresponding to the first frequency are

1.14, 0.80 and 0.53, respectively. The target frequency is selected as 6.17 Hz, and the standard and long filter sizes are set to 0.684 and 1.230 s, respectively.

Fig. 16 compares the reconstructed displacement with the calculated displacement from 5 to 8 s. Only the reconstruction results by the FFIR filter with the standard filter size are plotted because reconstruction results by the CFIR and FFIR filters with the long filter size appear identical for the scale used in the figure. Neither the amplitude error nor phase error is found in the reconstructed displacement. The details at the two peaks marked with circles in Fig. 16 are presented in Figs. 17 and 18 for the proposed filters with the standard and long filter sizes. The reconstruction errors at the peak shown in Fig. 17 by the FFIR filter for the standard and long filter sizes are evaluated as 0.8% and 0.6%, respectively, and those by the CFIR filter for the two filter sizes as 1.3% and 0.5%, respectively. The FFIR filter yields 1.8% and 2.9% error for the standard and long filter sizes at the peak shown in Fig. 18, respectively, and the CFIR filter yields 1.6% and 3.0% errors for the two filter sizes. The accuracy of the reconstructed displacement by the proposed filters at the peak shown in Fig. 18 almost coincides with the accuracy of the BEF transfer functions corresponding to the filter sizes at the target frequency. This is because the displacement components corresponding to the excitation frequencies have damped out, and only the displacement component corresponding to the fundamental frequency of the beam remains around the second peak.

To investigate the effect of noise on reconstruction results, displacement is reconstructed from noise-polluted accelerations and plotted in Fig. 19 together with those from noise-free accelerations. The noise-polluted accelerations are simulated by adding 5% random proportional noise generated with the uniform probability function to the accelerations calculated by the finite element analysis. The root mean square (rms) errors in the measured accelerations and the displacement reconstructed by the proposed FIR filter with the standard filter size are shown in Table 1. The 5% random proportional noise causes around 2.90% rms errors in the accelerations. The rms errors in the reconstructed displacements are around 4% for the forced vibration, and less than 2% for the free vibration, which demonstrates the robustness of the

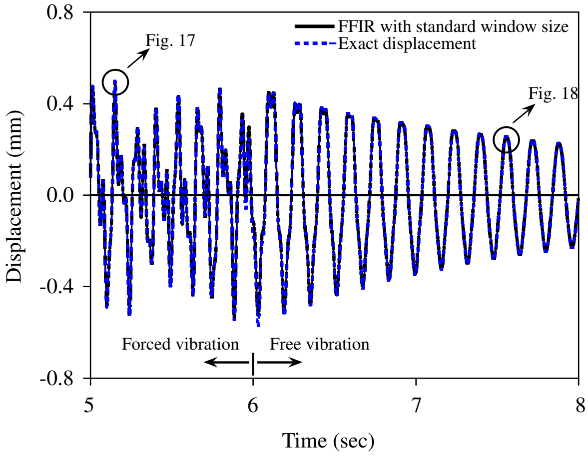

Fig. 16. Reconstructed displacement with noise-free data.

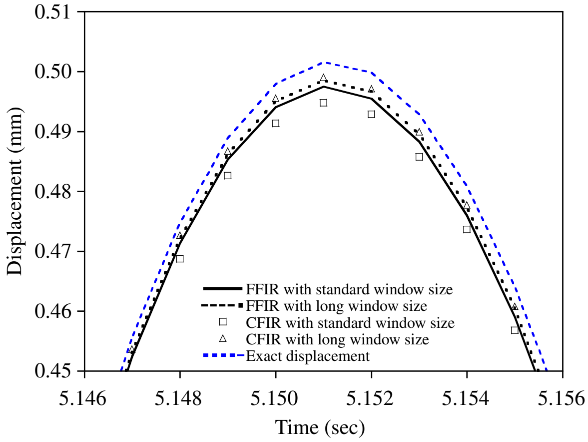

Fig. 17. Details of the reconstructed displacement during the forced vibration with noise-free data.

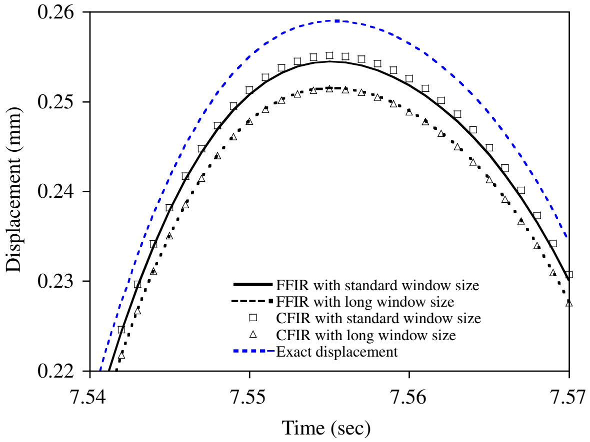

Fig. 18. Details of the reconstructed displacement during the free vibration with noise-free data.

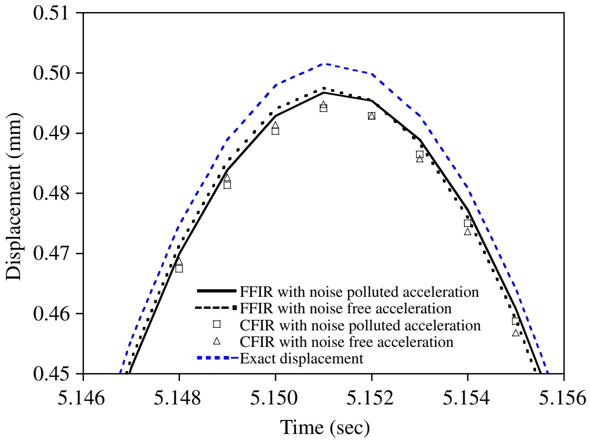

Fig. 19. Effect of measurement noise on reconstructed displacement during the forced vibration with the standard filter size.

Table 1
The rms errors in measured accelerations and reconstructed displacements of Example 1.

Type of vibration	Acceleration (%)		Reconstructed displacement (FFIR) (%)		Reconstructed displacement (CFIR) (%)	
	Noise-free	5% Noise	Noise-free	5% Noise	Noise-free	5% Noise
Forced vibration	0.00	2.90	1.73	3.98	1.79	4.02
Free vibration	0.00	2.85	1.75	1.93	1.51	1.72

proposed filters against noise. The reconstructed velocity from the noise-free accelerations is shown in Fig. 20. Only the reconstruction results obtained by the FFIR filter with the standard filter size are presented because differences between those with the long filter size and standard filter size are hardly noticeable for the scale of the figure. Although the details of the reconstructed velocity are not shown, the FFIR filter reconstructs the velocity at the same level of accuracy as the displacement.

4.2. Field test on a simply support railroad bridge

The acceleration and the displacement are measured at the center of a 40 m simply supported bridge on the Gyeongbu line of the Korea Train Express (KTX). The field experiment is conducted by the Steel Structure Research Laboratory of Research Institute of Industrial Science and Technology, Kyungki-do, Korea. The detailed figure on the experimental setup is given in Ref. [11]. The measurements are taken at a sampling rate of 1000 Hz while an actual train passes the bridge

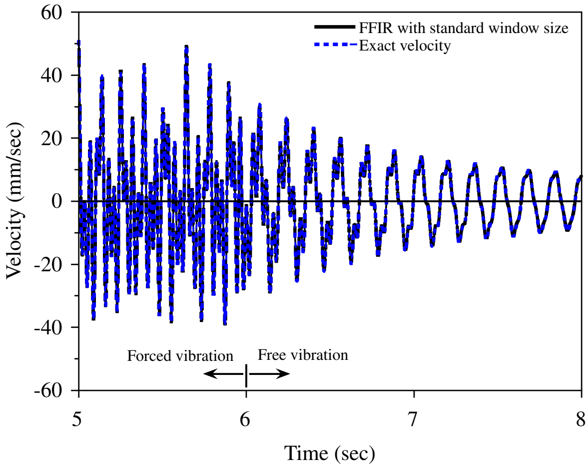

Fig. 20. Reconstructed velocity with noise-free data.

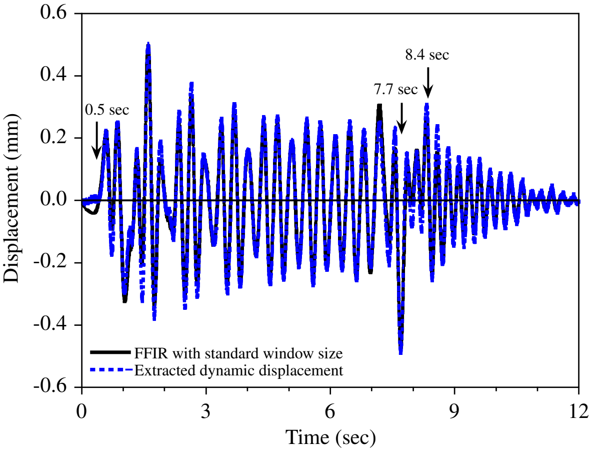

Fig. 21. Reconstructed and extracted dynamic displacement of the simply supported railway bridge with standard filter size.

during commercial operation. Three dominant frequencies of the bridge are identified as 2.86, 3.86 and 5.79 Hz from the FFT of the measured accelerations. The first and the second dominant frequency correspond to the excitation frequency induced by the moving train and the fundamental frequency of the beam, respectively. The target frequency is set to 2.86 Hz, and the standard filter size of 1.474 s is employed for the reconstruction. As the static displacement is included in the measured displacements, the pure dynamic displacement is extracted by the following formula proposed by Lee at al. [11]:

$$u_d(t) = u_m(t) - \frac{1}{T}\int_{t-T/2}^{t+T/2} u_m(\tau)\,\mathrm{d}\tau \tag{38}$$

Here $u_d(t)$, $u_m(t)$ and T are the extracted dynamic displacement, the measured displacement at time t and the target period, respectively. The train enters the bridge at 0.5 s, begins to exit the bridge from 7.7 s and completely leaves the bridge at 8.4 s. The aforementioned instances are not measured values but estimated ones based on the measured displacements.

Fig. 21 shows the extracted dynamic displacement by Eq. (38) and the reconstructed displacement by the FFIR filter. Results by the CFIR appear to be almost identical to those of the FFIR filter, and are not presented in the figure. When the train is on the bridge, the forced vibration is dominant. After the train leaves the bridge, the free vibration governs the responses of the bridge. The maximum differences between the reconstructed and extracted dynamic displacement at peaks are found as about 10% during the forced vibration, and those during the free vibration as about 25%. The details of reconstructed displacements by the CFIR filter, FFIR filter and the FDM-FIR filter proposed by Lee et al. [11] with the optimized filter size of 0.98 s are compared with the extracted dynamic displacement in Fig. 22. The three FIR filters yield almost identical results, and no noticeable difference is found in either the amplitude or the phase. Lee et al. point out that the discrepancies between the extracted and reconstructed displacements are caused by the extraction scheme.

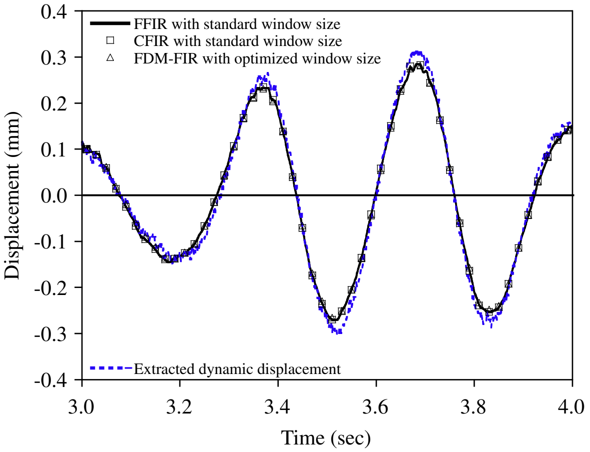

Fig. 22. Details of reconstructed and extracted dynamic displacement.

They demonstrate that the displacement component corresponding to the second dominant frequency is overestimated by 21% during the extraction, and that the reconstructed displacements represent actual dynamic displacements better than the extracted displacements. For details, refer to their work.

4.3. *Extraction of flutter derivatives from the reconstructed displacement responses*

This example is presented to demonstrate the overall accuracy of the reconstructed displacement by investigating the accuracy of dependent variables on displacement. The flutter derivatives of a section model representing a bridge deck system with plate girders are evaluated using the measured and reconstructed displacements. Measurements on displacement and acceleration taken from a wind tunnel test are utilized. The wind-induced motions of the deck in a long-span bridge generate self-excited forces that have strong influences on the stability of a bridge. Scanlan and Tomko [13] have formulated the flutter derivatives to express the self-excited forces in terms of the vertical and rotational motions of a bridge deck. The aeroelastic behaviors of a long-span bridge are foreseen with the flutter derivatives obtained from wind tunnel tests.

The experiment was performed by Kim and King at the Boundary Layer Wind Tunnel Laboratory of the University of Western Ontario in Ontario, Canada [18]. Experimental setups are shown in Fig. 23. The section model undergoes the vertical motion and the rotational motion with respect to the center of rotation of the cross section. The section model is rigidly attached to the two rigid beams supported by two springs at each end. Acceleration and displacement are measured at two points located symmetrically 38.1 cm away from the center of rotation of the section model in each rigid beam with the sampling frequency of 100 Hz. The vertical displacements and the rotation angles of the cross section are obtained by averaging the displacements measured at the four sensors and two differential displacements of two sensors in each rigid beam, respectively. The displacement and the velocity are reconstructed from accelerations measured at each accelerometer by the FFIR filter with the standard filter size, and the aforementioned averaging scheme is employed.

Sudden release tests are carried out for 16 different wind speeds, and 20 trials are performed for each wind speed. The vibration of the section model is initiated by the sudden release of the rigid beams from an initial position. Table 2 shows the fundamental dynamic characteristics of the section model for each wind speed. Two dominant frequencies are found for each wind speed by the FFT of measured accelerations. The low and high frequencies correspond to the vertical and rotational motion of the section model, respectively, and the low frequencies are selected as the target frequencies for the reconstruction. The frequencies and filter sizes presented in the table are the averaged values obtained at the four sensors in the 20 trials.

The reconstructed displacements agree well with measured displacements for all wind speeds except near the releasing point. Fig. 24 shows the reconstructed and measured vertical displacement of the section model for the first trial of case 16, which yields the largest reconstruction errors compared to the other wind speeds. Although case 16 is considered to be the worst case in the reconstruction of displacement, the reconstructed displacement nonetheless agrees well with the measured displacement. Some discrepancies between the measured and reconstructed displacement are observed for 0.69 s after the release of the section model. This is because measured accelerations before and after the sudden release are simultaneously included in a time window up to 0.69 s, which is the equivalent of half the filter size. This phenomenon is a fundamental property of the FIR filter, and commonly observed at all wind speeds.

The flutter derivatives are extracted by solving an inverse problem with the prediction-error minimization method (PEM) [19] in the MATLAB library based on a state-space formulation [20]. The extraction is performed with displacement data for the time duration shown in Table 2 starting after one period of the vertical motion from the sudden release. For the

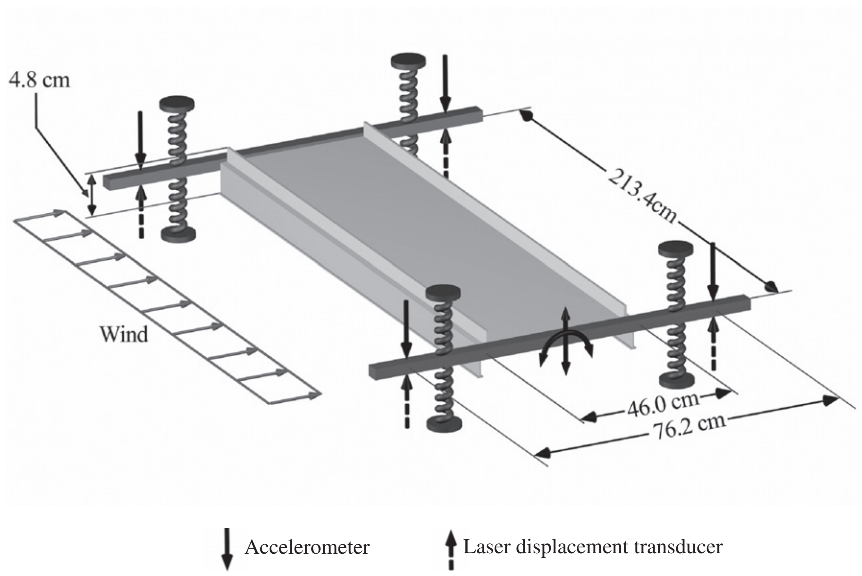

Mass per unit length: 3.64 (kg/m)
Mass moment of inertia per unit length: 0.102 (kg-m^2/m)
Air density: 1.25 (kg/ m^3)

Fig. 23. Experimental setup of the plate girder section for wind tunnel test.

Table 2
Wind speed, identified frequencies and other parameters of Example 3.

Case	Wind speed (m/s)	Identified frequency (Hz)		Filter size (s)	Data length[a] (s)	No. of successful trials
		Vertical	Rotational			
1	0.000	3.052	5.127	1.381	3.280 (v)	19
2	0.679	3.047	5.136	1.383	3.280 (v)	11
3	1.679	3.059	5.135	1.378	3.270 (v)	18
4	2.647	3.066	5.082	1.375	3.260 (v)	9
5	2.964	3.062	5.110	1.377	3.270 (v)	16
6	3.620	3.022	5.153	1.395	3.310 (v)	16
7	3.935	3.008	5.204	1.401	3.320 (v)	20
8	4.265	3.031	5.162	1.391	3.100 (r)	12
9	4.601	3.055	5.175	1.380	2.900 (r)	14
10	4.911	3.108	5.250	1.356	2.490 (r)	8
11	5.243	3.140	5.166	1.342	2.090 (r)	14
12	5.562	3.204	5.145	1.316	1.230 (r)	11
13	6.517	3.214	4.752	1.312	1.100 (r)	15
14	7.495	3.374	4.674	1.249	2.200 (v)	16
15	8.162	3.273	4.612	1.288	1.610 (v)	5
16	8.875	3.308	4.638	1.274	1.210 (v)	4

[a] (v) and (r) indicates the vertical motion and the rotational motion.

slower wind speeds up to case 7, the time duration corresponds to 10 periods of the vertical motion. Since dynamic responses damp out quickly for higher wind speeds, the time duration from case 8 is determined by the earlier instance when either the vertical or rotational motion of the section model disappears. The letter in the parenthesis of the data length column in Table 2 indicates the direction of motion that disappears first.

The PEM sometimes fails to converge or yield physically meaningful results due to the ill-posedness of the inverse problem. The flutter derivatives presented in this paper are the averages of values obtained in successful trials for which the PEM yields physically meaningful results for both the reconstructed and measured displacement. The number of successful trials for each wind speed is shown in the last column of Table 2. It should be noted that velocity and displacement are utilized simultaneously in the PEM to improve the accuracy and stability of results for noisy measurement. Since, however, displacement is measured with very high accuracy in a wind tunnel test, the results of the extraction with and without the reconstructed velocity are almost identical, and thus are not presented.

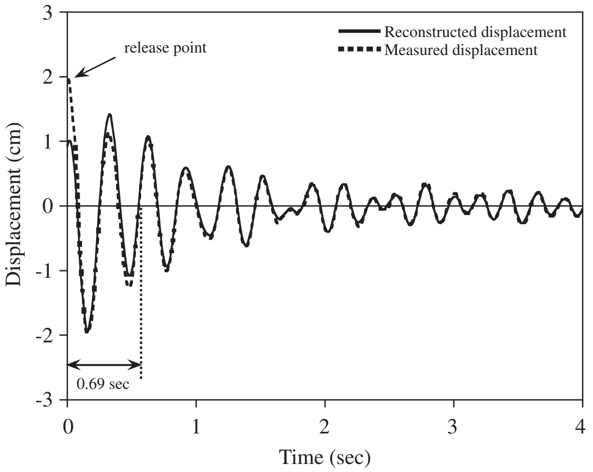

Fig. 24. Reconstructed displacement in the vertical direction for the highest wind speed.

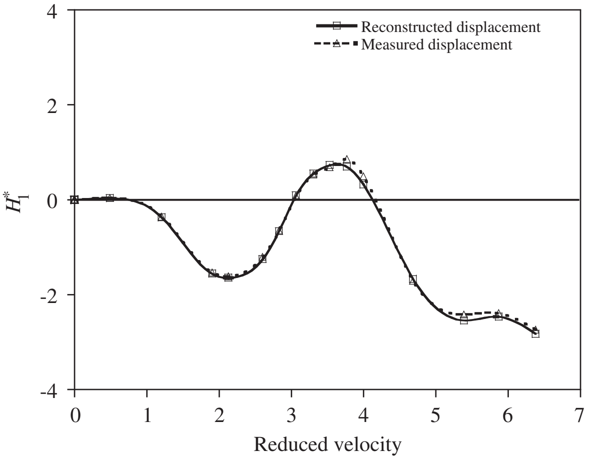

Fig. 25. Vertical direct flutter coefficient, H_1^*.

Eight flutter derivatives are defined for a section model with two dofs under wind actions. Among them, two direct derivatives H_1^* and A_2^* are of great importance in the design of a cross section for a long-span bridge [3,13]. The former relates the lift force to the vertical velocity and the latter expresses the torsional moment in terms of the rotational velocity of the section model. Moreover, the two derivatives are the most influential variables in estimating the aerodynamic damping of a long-span bridge, which governs the stability of a cross section against wind actions. Figs. 25 and 26 show the direct flutter derivatives extracted from the reconstructed displacements along with those from the measured displacements. The centered symbols and the lines represent the extracted derivatives at the wind speeds shown in Table 2, and the cubic spline fits of them, respectively. In the figures, the flutter derivatives are plotted against the non-dimensional reduced velocity defined as follows:

$$\tilde{V}_m = \frac{V_w}{Bf_m}, \quad m = \text{vertical, rotational} \tag{39}$$

Here, subscript m indicates the direction of a motion, and $\tilde{V}_m$, V_w, B and f_m are the reduced wind speed, the real wind speed, width of the section model and the frequency, respectively.

The two sets of flutter derivatives agree very well with each other for all wind speeds. No noticeable differences are found in the other flutter derivatives that are not presented here. This implies that the flutter derivatives may be extracted based on the reconstructed displacements from accelerations measured with accelerometers rather than measured displacements with displacement transducers. Accordingly, a strong potential feasibility of utilizing accelerometers in assessing aerodynamic and aeroelastic characteristics of long-span bridges in service are recognized.

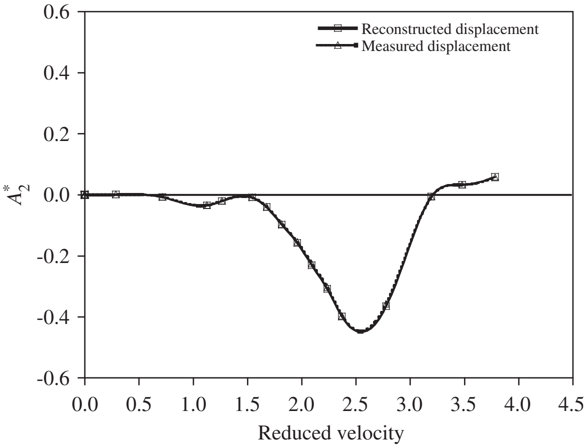

Fig. 26. Rotational direct flutter coefficient, A_2^*.

5. Summary and conclusion

This paper proposes two types of FIR filters, the CFIR and FFIR filter, to reconstruct displacement from measured accelerations. The BEF transfer function is derived by taking the variation of the minimization problem that defines an inverse problem for the reconstruction of displacement. The regularization factor in the inverse problem is determined with the desired accuracy at the target frequency. The CFIR filter directly approximates the BEF transfer function in the frequency domain by the truncated Fourier series, while the FFIR filter is obtained by discretizing the variational statement of the minimization problem with the standard FEM for beam problems. The Hermitian shape function is utilized to interpolate displacement in each finite element. Velocity as well as displacement can be reconstructed simultaneously from the same measurement.

The proposed filters are capable of suppressing the low frequency noises below the target frequency, and reconstructing displacement accurately above the target frequency. The longer filter size results in smaller rippling amplitude in both filters. The CFIR filter exhibits a uniform frequency response from the target frequency to the Nyquist frequency in case the filter size is set to either the standard or long filter size. The filter sizes other than the two filter sizes cause diverging rippling amplitudes in the transfer function of the CFIR filter, which may be considered to be the one shortcoming of the CFIR filter. On the other hand, the FFIR filter size can be adjusted freely as needed in applications and the rippling amplitude damps out quickly for all filter sizes. Although the accuracy of the FFIR filter deteriorates in higher frequency ranges, the overall performance is not affected seriously because the high frequency contents in measured accelerations contribute little to the reconstructed displacement. From the aforementioned facts, it may be concluded that the CFIR filter is a good choice for the reconstruction in systems with a wide frequency spectrum while the FFIR filter is suitable for low-frequency dominant systems. To reconstruct velocity as well as displacement, however, the FFIR filter should be employed.

Three examples are presented to verify the proposed FIR filters. In the numerical simulation study and field experiment, the CFIR and the FFIR filter yield very accurate displacement, and exhibit robust behaviors against measurement noises. In the last example, the flutter derivatives for the section model of a bridge deck system with plate girders are identified by the reconstructed displacement, and are compared with those by measured displacement. Both the identified derivatives show good agreement with each other. Therefore, the proposed FIR filters can be applied to the identification of the flutter derivatives of long-span cable-supported bridges in service, in which the measurements of displacement are considered to be one of the major obstacles. It is believed that the proposed FIR filters provide accurate and reliable alternatives to direct measurement of dynamic displacements, which is costly, difficult and almost impossible, especially for large-scale structures.

Acknowledgement

This research was supported by the grant (09CCTI-A052531-02-000000) from the Ministry of Land, Transport and Maritime of Korean government through the Core Research Institute at Seoul National University for Core Engineering Technology Development of Super Long Span Bridge R&D Center. The authors would like to express their sincere gratitude to Steel Structure Research Laboratory of Research Institute of Industrial Science and Technology and to Korea Wind Engineering Research Center at Mokpo National University for releasing valuable experimental data to them. The authors wish to thank Prof. S.D. Kwon at Chonbuk National University, Jeonju, Korea for his valuable advice on the evaluation of flutter derivatives.

References

[1] H. Sohn, C.R. Farrar, F.M. Hemez, D.D. Shunk, S.W. Stinemates, B.R. Nadler, J.J. Czarnecki, A review of structural health monitoring literature: 1996–2001, Los Alamos National Laboratory report LA-13976-MS, 2004.

[2] G.W. Housner, L.A. Bergman, T.K. Caughey, A.G. Chassiakos, R.O. Claus, S.F. Masri, R.E. Skelton, T.T. Soong, B.F. Spencer, J.T.P. Yao, Structural control: past, present, and future, *Journal of Engineering Mechanics* 123 (1997) 897–971.

[3] P.P. Sakar, N.P. Jones, R.H. Scanlan, Identification of aeroelastic parameters of flexible bridges, *Journal of Engineering Mechanics, ASCE* 120 (8) (1994) 1718–1741.

[4] H.P. Gavin, R. Morales, K. Reilly, Drift-free integrators, *Review of Scientific Instruments* 69 (5) (1998) 2171–2175.

[5] L.R. Rabiner, B. Gold, in: *Theory and Application of Digital Signal Processing*, Prentice-Hall, Englewood Cliffs, NJ, 1975.

[6] R.W. Hamming, in: *Digital Filters*, 3rd ed., Prentice-Hall, Englewood Cliffs, NJ, 1989.

[7] B. Kumar, D.R. Choudhury, A. Kumar, On the design of linear phase, FIR Integrators for midband frequencies, *IEEE Transactions on Signal Processing* 44 (10) (1996) 2391–2395.

[8] D.M. Boore,C.D. Stephens, W.B. Joyner, Comments on baseline correction of digital strong-motion data: example from the 1999 Hector Mine, California, Earthquake, Bulletin of the Seismological Society of America 1997; 87: 932-944.

[9] L. Bardella, A. Carini, F. Genna, Time integration errors and some new functionals for the dynamics of a free mass, *Computers & Structures* 81 (2003) 2361–2372.

[10] A. Smyth, M. Wu, Multi-rate Kalman filtering for the data fusion of displacement and acceleration response measurements in dynamic system monitoring, *Mechanical Systems and Signal Processing* 21 (2007) 706–723.

[11] H.S. Lee, Y.H. Hong, H.W. Park, Design of an FIR filter for the displacement reconstruction using measured acceleration in low-frequency dominant structures, *International Journal for Numerical Methods in Engineering* 82 (2010) 403–434.

[12] M.I. Hetenyi, in: *Beams on elastic foundation: theory with applications in the fields of civil and mechanical engineering*, University of Michigan, 1946.

[13] R.H. Scanlan, J.J. Tomko, Airfoil and bridge deck flutter derivatives, *Journal of the Engineering Mechanics Division, ASCE* 97 (1971) 1717–1737.

[14] A.K. Chopra, in: *Dynamics of Structures: Theory and Applications to Earthquake Engineering*, 2nd ed., Prentice-Hall, Upper Saddle River, NJ, 2001.

[15] A. Cheng, D.T. Cheng, Heritage and early history of the boundary value element method, *Engineering Analysis with Boundary Element* 29 (2005) 268–302.

[16] S.K. Park, H.W. Park, S.B. Shin, H.S. Lee, Detection of abrupt structural damage induced by an earthquake using time-window technique, *Computers & Structures* 86 (2008) 1253–1265.

[17] T.J.R. Hughes, in: *The Finite Element Method: Linear Static and Dynamic Finite Element Analysis*, Prentice-Hall, Englewood Cliffs, NJ, 1987.

[18] J.D. Kim, J.P.C. King, The development of wind tunnel test technique for an aeroelastic buffeting analysis of long-span bridges, BLWTL-SS19-2007-DRAFT report submitted to Korea Wind Engineering Research Center, The Boundary Layer Wind Tunnel Laboratory of The University of Western Ontario, 2007.

[19] L. Ljung, in: *System Identification: Theory for the User*, 2nd ed., Prentice-Hall, Upper Saddle River, NJ, 1999.

[20] MATLAB v 7.9.0(R2009b), Help Browser.